Modelling the Gamma-ray Morphology of the Supernova Remnant W28

Sabrina Einecke,[a,*] **Gavin Rowell,**[a] **Jemma Pilossof,**[a] **Michael Burton**[b] **and Kerem Cubuk**[b]

[a]*The University of Adelaide, School of Physics, Chemistry and Earth Sciences*
Adelaide, Australia

[b]*Armagh Observatory and Planetarium, College Hill,*
Armagh, United Kingdom

E-mail: sabrina.einecke@adelaide.edu.au

Gamma-ray emission in the GeV and TeV energy regime has been detected towards the old supernova remnant (SNR) W28. This object is a prime candidate for the study of cosmic-ray acceleration and diffusion, as the established adjacent molecular clouds provide target material for gamma-ray production and, due to its age, most particles have already escaped the shock front into the interstellar medium. While gamma-ray spectra from different regions around the SNR have been successfully modelled by several authors, the predicted morphology is still lacking, which prevents us from fully understanding the details of the particle acceleration and transport. High-energy gamma rays can be produced by the decay of neutral pions created in inelastic collisions of cosmic rays and the interstellar gas. For accurate modelling of morphology, we need to know the location of cosmic rays and the interstellar gas in 3D, as small changes in relative position cause large differences in morphology.

In this contribution, we will introduce our novel 3D modelling and present the gamma-ray morphology around the SNR W28 using arcminute-scale molecular hydrogen gas distributions from the Mopra CO survey. We will also discuss our optimisation procedure to determine the SNR, diffusion and gas properties to reproduce spatial and spectral gamma-ray observations from HESS and *Fermi*-LAT.

*Speaker

PoS(ICRC2023)923

1. Introduction

Cosmic rays (CRs) are accelerated in shock fronts of supernova remnants (SNRs) and, depending on their energy, eventually escape and diffuse into the surrounding medium. Differentiating between hadronic and leptonic CRs is typically challenging; however, we can exploit the fact that electrons lose their energy much more rapidly through radiative cooling than protons. Consequently, only protons are able to diffuse over considerable distances, on the order of tens of parsecs, and produce gamma-ray emission away from the SNR shell.

The mixed-morphology SNR W28 (G6.4-0.1) has long been a popular subject of many studies, as its characteristics and environment provide an ideal base. Due to the SNR's old age of 35–150 kyrs [1], most of its CRs have escaped into the surrounding interstellar medium (ISM), electrons would have lost most of their energy, and TeV protons that escaped during an early stage of the SNR evolution would have diffused a substantial distance. The interaction between W28 and ambient matter is established through the presence of numerous 1720 MHz masers [2], very dense interstellar shocked gas [3] and an expanding atomic hydrogen (HI) void [4]. The interstellar gas provides target material for gamma-ray production, while adjacent molecular clouds allow searches for spatial correlations with gamma-ray emission. Indeed, *Fermi*-LAT [5, 6] and HESS [7] detected extended GeV and TeV gamma-ray emission, respectively, with distinct energy-dependent morphologies. The spatial match of TeV gamma rays with molecular clouds beyond 10 pc from the shell, suggests that hadronic CRs are accelerated in W28. In GeV gamma rays, only the closest molecular clouds are illuminated, which can be explained by low-energy CRs escaping much later and then having less time to diffuse far. The proposed distance of 1.8–3.3 kpc places W28 relatively close to Earth, allowing us to observe bright emission and resolve distinct features.

Gamma-ray spectra from different sky regions in the W28 field have been successfully modelled by several authors e.g. [5, 6]). However, to investigate particle acceleration, diffusion and the environment of W28 in detail, we also need to be able to model the energy-dependent morphology, requiring models of the CR density and ISM hydrogen density in 3D.

2. Observations

We will compare our modelled gamma-ray spectra and energy-dependent gamma-ray distributions to observations obtained with *Fermi*-LAT and HESS. Our model to produce gamma rays via pion decay requires a model of the hydrogen number density in 3D, which is based on carbon monoxide ^{12}CO(1–0) observations with the Mopra radio telescope.

2.1 Very-High-Energy Gamma Rays

HESS discovered the TeV gamma-ray sources HESS J1801-233 and HESS J1800-240A, B and C in ~42 hours of observations of the W28 field from 2004 to 2006 [7]. The location and extension σ_{src} of each source were obtained by fitting 2D Gaussians to the obtained excess count maps. TeV photon spectra were then extracted from circular regions of radius $\sqrt{0.1^{\circ 2} + \sigma_{\mathrm{src}}^2}$. Figure 1 shows the integral gamma-ray flux above 1 TeV from the HESS Galactic Plane Survey [8], along with the significance contours from [7] and [8].
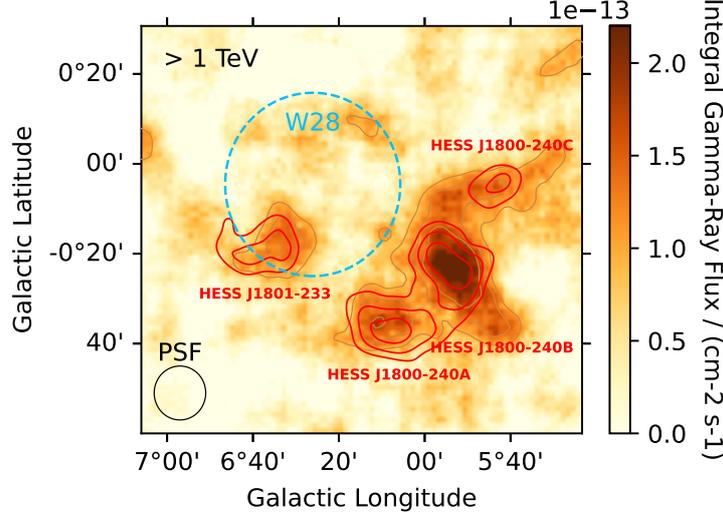
Figure 1: Integral gamma-ray emission above 1 TeV obtained with HESS [8]. The $(4, 5, 6)\,\sigma$ significance contours (red) from [7] highlight the four TeV gamma-ray sources. The current extension of W28 (blue circle) shows that CRs must have escaped to produce the gamma-ray emission of HESS J1800-240.

2.2 High-Energy Gamma Rays

We analysed ~14.5 years of data collected with *Fermi*-LAT from 2008 to 2023. Our event selection comprised Clean-type events, excluding events with zenith angles $> 90°$ and rocking angles $< 52°$ to decrease the effects of terrestrial albedo gamma rays. The data analysis was performed with `Fermitools 2.2` along with the instrument response function `P8R3_CLEAN_V3`. The background model included the Galactic diffuse background (`gll_iem_v07.fits`), the isotropic background (`iso_P8R3_*_V3_v1.txt`) and all sources in the latest *Fermi*-LAT catalogue (4FGL-DR3 [9]) within $30°$ of W28. All 4FGL sources, except for 4FGL J1757.9-2419, within a $1°$ radius of W28 were replaced by the four spatial models for HESS J1801-233 and HESS J1800-240 from [7].

We generated a series of test statistic (TS) maps (see Figure 2) using only PSF3-type events to achieve the best angular resolution (68% containment radius of below $0.4°$). The energy-dependent morphology in GeV gamma rays is clearly evident. For producing the spectral energy distributions, FRONT-type events were extracted for all four HESS sources from the same regions as defined in [7]. In each energy bin, we required a minimum TS value of 9. Systematic uncertainties, associated with the Galactic diffuse emission and inaccuracies in the effective area A_{eff}, were calculated by varying the Galactic diffuse background normalisation by $\pm 5\%$ and scaling the effective area with its systematic uncertainty ϵ via $(1 \pm \epsilon(E))\,A_{\text{eff}}(E)$.

2.3 Interstellar Medium and Molecular Clouds

To trace the ISM and molecular clouds, we use arcminute-scale observations of $^{12}\text{CO}(1\text{--}0)$ from the Mopra Southern Galactic Plane carbon monoxide (CO) survey. Data were taken at 0.6 arcmin spatial and 0.1 km/s spectral resolution, and were reduced using the ATNF packages `livedata` and `gridzilla`, similar to the strategy described in [10]. The resulting data products are `fits` cubes in position-position-velocity (PPV) space.
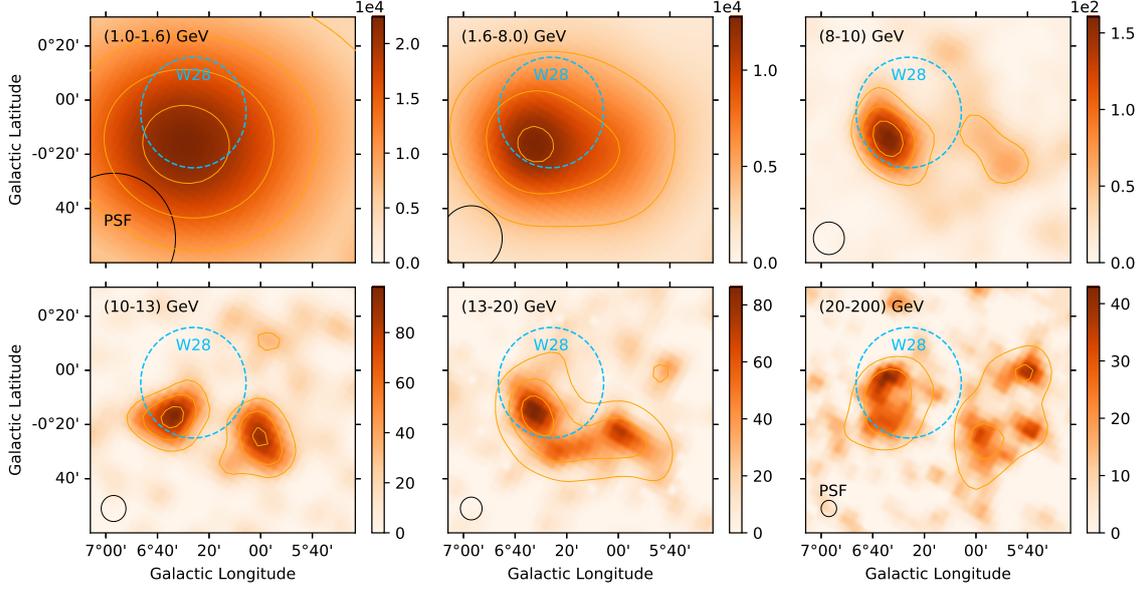
Figure 2: Test Statistic (TS) maps obtained with *Fermi*-LAT for different energy bands. Note that different energy bands feature different angular resolutions, as visualised by the PSF circle (68% containment for PSF3-type events). `https://www.slac.stanford.edu/exp/glast/groups/canda/lat_Performance.html`

3. Modelling

Here we present a novel approach to derive unprecedented models of energy-dependent CR, ISM and gamma-ray distributions in 3D. As small changes in relative position between CR and ISM density can cause large differences in the resulting gamma-ray distribution, an accurate modelling of the morphology needs to be performed in 3D. However, deriving these 3D distributions comes with many challenges, as discussed in the following subsections. An overview of the importance and challenges of 3D modelling and the developed software framework is presented in [11].

3.1 Cosmic-Ray Protons

For our model of the CR proton density distribution $J_p \left(E_p, R, t \right)$, we place W28 as the accelerator with age T at distance D from Earth. We model the Sedov phase of the SNR evolution, where previously accelerated particles with energy E_p escape the shock front with radius $R_{esc}(t_{esc}(E_p))$ [12] at a time $t_{esc}(E_p)$ [13] after the supernova (SN) explosion. The shock front is expanding with time, and high-energy particles escape early close to the centre of the SNR, while low-energy particles escape later further away from the centre. We assume that the accelerator is impulsively (at one specific time only) injecting particles into the ISM with a power law spectrum with an exponential cutoff at an energy E_{cut} (to account for effects due to an older accelerator):

$$N(E_p) = N_0 \cdot \left(\frac{E_p}{E_0} \right)^{-\alpha} \cdot \exp \left(-\frac{E}{E_{cut}} \right) . \tag{1}$$

The total number of particles N_0 is derived from the available energy budget $W_p = \eta \, E_{SN}$, defined as the fraction η of the SN explosion energy E_{SN} that goes into CRs. For modelling the particle

transport, we only consider radiative losses (which are small in relevant time scales) and diffusion in an isotropic, homogeneous medium, where the diffusion coefficient does not depend on direction and does not vary in space. This allows us to use an analytical solution to the transport equation. Our solution (see [11]) is based on [14], but includes particles distributed according to Equation 3.1, which are injected at different times and locations dependent on the particle's energy. This solution produces similar results as in [17]. To also include the particles that have not yet escaped and are still confined within the SNR, we simply assume that 68% of the particles are uniformly distributed in a shell of width w_{shell} and the remaining ones uniformly distributed in the inner sphere.

3.2 Interstellar Medium

One of the major challenges in our modelling is the derivation of the ISM distribution in position-position-position (PPP) space (sky coordinates and distances to Earth). Measurements tracing the ISM always come in position-position-velocity (PPV) space (sky coordinates and line-of-sight Doppler velocities) and need to be transformed. Models of the Milky Way's rotation provide a method to translate radial velocities to kinematic distances; however, for most cases ambiguous solutions of a 'near' and a 'far' distance exist. Another problem is that the measured velocities are a combination of radial motions and local motions of the gas. As we cannot measure the local motions of the gas to subtract, a large uncertainty on the distance arises (in the order of hundreds of parsecs). Additionally, the small scales of cloud depths in the order of a few parsec cannot be accommodated when simply applying the above translation.

We developed a novel approach that allows the creation of a PPP cube with any user-specified distance axis, capable of separating overlapping clouds and that enables clouds to be moved individually along the distance axis for optimisation purposes. In a first step, we perform a Gaussian decomposition with `GaussPy+` [16], which decomposes the emission line spectrum of each sky pixel into individual velocity components approximated by Gaussians. The package performs a two-phase denoising to account for broad and narrow linewidths before calculating the derivatives to automatically determine the number of components in each spectrum. The decomposition is very sensitive to the settings of the denoising and therefore a supervised machine learning technique is incorporated to determine them appropriately. Additionally, it includes an iterative re-fitting routine, improving the decomposition by requiring similar results in neighbouring sky pixels. The output is a table listing the parameters of each Gaussian component.

In the next step, we determine a label for each component, specifying to which molecular cloud it belongs to. For this purpose, we prepare a new PPV cube, where we place the integrated Gaussian component at its derived velocity, followed by a 3D Gaussian smoothing. This cube is then used for a hierarchical clustering performed with `astrodendro`. We transfer the obtained labels of the identified clusters to the table of Gaussians components. Based on this table, we can place each cloud at a specified distance in a PPP cube. The last step involves transforming the integrated brightness temperature W_{CO} to a hydrogen number density $n_{\text{H2}} = X_{\text{CO}} W_{\text{CO}}$. The total hydrogen number density n_{H} consist of contributions from molecular and atomic hydrogen: $n_{\text{H}} = n_{\text{HI}} + 2n_{\text{H2}}$. In the following, we neglect the atomic component, as the upper limit of n_{HI} in the vicinity of W28 is $(1–2)/\text{cm}^3$ [4], orders of magnitude below the contributions from molecular hydrogen.

Based on many previous studies of the W28 region [3–7, 15], we choose a velocity range of $(0–30)$ km/s to perform the clustering. The identified 3D clusters are illustrated in Figure 3 as
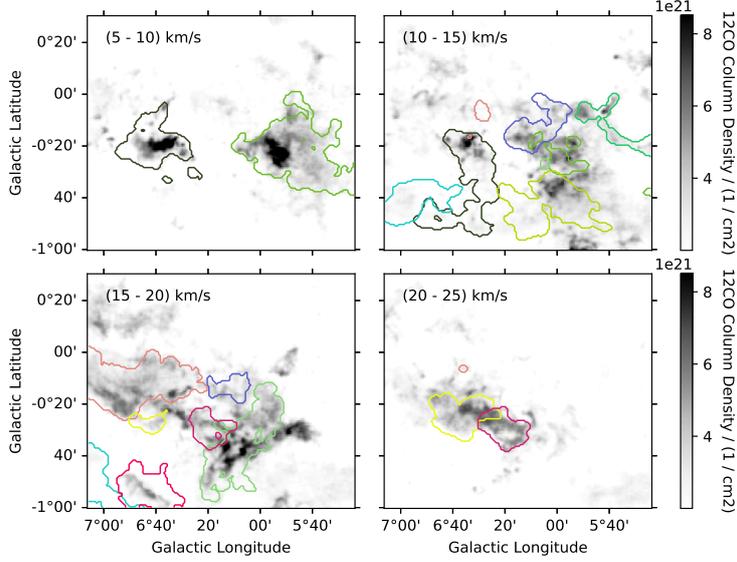
Figure 3: Mopra carbon monoxide ^{12}CO column density distribution in different velocity ranges, along with the obtained clusters. Note that the corresponding number density distributions in 3D are used in our model and that also the clusters are 3D objects. For illustration purposes, we show here the outermost extension of each cluster in its corresponding velocity range.

Table 1: Properties of clouds identified in the clustering.

Cloud ID	GLON / deg	GLAT / deg	Velocity / (km/s)	Components	Mass / (1e^3 M$_\odot$)	Y/N
1	5.8 ± 0.4	-0.4 ± 0.3	8.7 ± 2.0	1510	19.9	Y
2	6.6 ± 0.3	-0.4 ± 0.5	10.2 ± 5.3	1239	16.3	Y
3	6.0 ± 0.3	-0.7 ± 0.2	11.4 ± 1.4	794	8.7	Y
4	5.7 ± 0.3	-0.2 ± 0.2	12.6 ± 1.0	234	2.8	Y
5	6.1 ± 0.2	-0.2 ± 0.2	14.3 ± 2.3	434	6.7	Y
6	7.0 ± 0.2	-0.7 ± 0.3	14.4 ± 4.1	641	7.3	N
7	6.1 ± 0.3	-0.6 ± 0.4	17.9 ± 2.0	946	13.1	Y
8	6.8 ± 0.4	-0.2 ± 0.2	18.1 ± 1.9	1297	20.1	N
9	6.7 ± 0.2	-0.9 ± 0.1	18.6 ± 0.8	537	3.5	N
10	6.3 ± 0.2	-0.5 ± 0.1	20.5 ± 1.1	319	5.6	Y
11	6.6 ± 0.2	-0.4 ± 0.1	21.8 ± 3.0	577	6.4	Y

2D outlines and their properties are summarised in Table 1. We excluded some of the clouds in our modelling (indicated in the table by Y/N), as they are clearly not responsible for the observed gamma-ray emission. We construct a PPP cube with a distance resolution of 1 pc, a total depth of 300 pc and centred at a distance d_0 of 2 kpc. In a first attempt, we set the distance d_c of an individual cloud dependent on the cloud's median velocity v_c according to $d_c = d_0 + \frac{dl_{cube}}{dv_{cube}}(v_c - v_0)$ with a velocity v_0 at the centre of the cube. The clouds are spread over $dv_{cube} \approx 15$ km/s and we will distribute them over a distance of dl_{cube} (e.g. 100 pc). The distance d of an arbitrary pixel of a cloud is then $d = d_c + \frac{dl_c}{dv_c}(v_c - v_0)$. Assuming a typical cloud depth of 10 pc and variation of velocities in a cloud of 2 km/s, we choose $\frac{dl_c}{dv_c} = 10$ pc / 2 km/s.
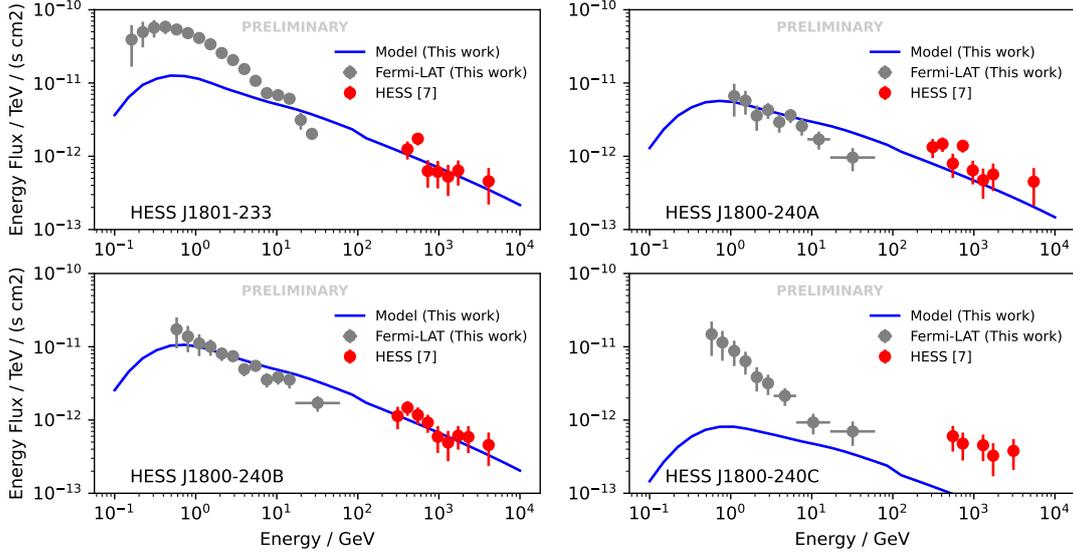
Figure 4: Example of our modelled gamma-ray spectra. The model parameters are as follows: T =35 kyr, χ =0.5, B =10 uG, δ=0.3, $E_{max} = E_{cut}$ =5 PeV, E_{SN} = $1e51$ erg, η =0.3, M_{ej}=1.4 M$_\odot$, α =2.1.

Our resulting hydrogen number densities are in the order of $(1e^3$–$1e^4)$ cm^{-3}, consistent with the ones determined e.g. in [3, 7] for the W28 region. However, dense cores (as detected in [15]) were not included in our model, as ^{12}CO is not able to trace these densities due to its abundance and becoming optically thick.

3.3 Gamma Rays

In our scenario, high-energy gamma rays are produced by the decay of neutral pions created in inelastic collisions of CR protons and protons in the interstellar gas. The gamma-ray flux from a region of volume V with hydrogen number density n_H at distance D from Earth, is calculated with the following equation:

$$F(E_g) = \frac{c\, n_H\, V}{4\pi D^2} \int_{E_g}^{\infty} \frac{d\sigma}{dE_g} \left(T_p, E_g\right)\, J_p(T_p)\, dT_p \,. \tag{2}$$

We utilise the parameterisation of the gamma-ray differential cross section $d\sigma/dE_g$ from [18], which is based on Monte Carlo simulations and data on proton-proton interactions.

4. Results

We tested a range of parameters describing the properties of the accelerator, its environment, the particle transport and different distances of the clouds. Figure 4 shows an example of the modelled spectra for each HESS source in comparison to the HESS and *Fermi*-LAT observations. Figure 5 shows example distributions of the integral gamma-ray flux above 1 TeV. To compare to Figure 1, we applied scaling factors to account for different pixel sizes and HESS's oversampling.
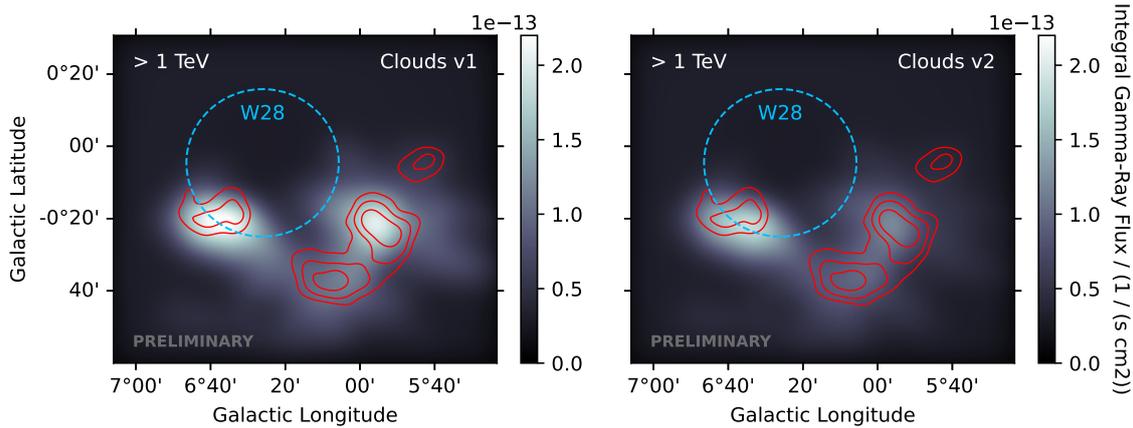
Figure 5: Examples of our modelled TeV gamma-ray distribution for different distributions of the clouds.

Acknowledgments

References

[1] V. Kaspi et al., *Astrophys. J. L.* **409** (1993) L60

[2] M. Claussen, D. Frail, W. Goss and R. Gaume, *Astrophys. J.* **489** (1997) 143

[3] W. Reach, J. Rho and T.H. Jarrett, *Astrophys. J.* **618** (2005) 297

[4] P. Velázquez, G. Dubner, W. Goss and A. Green, *Astro. J.* **124** (2002) 2145

[5] Y. Cui, P. Yeung, T. Tam and G. Pühlhofer, *Astrophys. J.* **860** (2018) 69

[6] Y. Hanabata et al., *Astrophys. J.* **786** (2014) 145

[7] F. Aharonian et al., *Astron. Astrophys.* **481** (2008) 401

[8] H.E.S.S. Collaboration et al., *Astron. Astrophys.* **612** (2018) A1

[9] S. Abdollahi et al., *Astrophys. J. Suppl. Ser.* **260** (2022) 53

[10] C. Braiding et al., *Publ. Astron. Soc. Australia* **35** (2018), E029

[11] S. Einecke, G. Rowell, R. Burley, R. König, T. Collins and F. Voisin, PoS(ICRC2023)925 (2023)

[12] J. Truelove and C. McKee, *Astrophys. J. Suppl. Ser.* **120** (1999) 299

[13] S. Gabici, F. Aharonian and S. Casanova, *Mon. Not. R. Astron Soc.* **396** (2009) 1629

[14] F. Aharonian and A. Atoyan, *Astron. Astrophys.* **309** (1996) 917

[15] B. Nicholas et al., *Mon. Not. R. Astron Soc.* **411** (2011) 1367

[16] M. Riener et al., *Astron. Astrophys.* **628** (2019) A78

[17] Y. Ohira, K. Murase and R. Yamazaki, *Mon. Not. R. Astron Soc.* **410** (2010) 1577

[18] E. Kafexhiu, F. Aharonian, A. Taylor and G. Vila, *Phys. Rev. D* **90** (2014) 123014